Biomedical Optics EXPRESS

Spatial Light Interference Microscopy (SLIM) using twisted-nematic liquid-crystal modulation

Tan H. Nguyen and Gabriel Popescu*

Quantitative Light Imaging Laboratory, Department of Electrical and Computer Engineering, Beckman Institute for Advanced Science & Technology, University of Illinois at Urbana-Champaign, Illinois 61801, USA
*gpopescu@illinois.edu

Abstract: We report the use of a twisted nematic liquid-crystal spatial light modulator (TNLC-SLM) for quantitative phase imaging. The experimental setup is a new implementation of the SLIM principle, which is a phase shifting, white light method for quantitative phase imaging. The approach is based on switching between the phase and amplitude modulation modes of the SLM. Our system is able to deliver a 0.99 nm spatial and 1.33 nm temporal pathlength sensitivity while retaining the optical transverse resolution. The system is implemented as an additional module mounted to a conventional microscope, which makes the system very easy to deploy and integrate with other imaging modalities.

©2013 Optical Society of America

OCIS codes: (180.0180) Microscopy; (180.3170) Interference microscopy; (070.6120) Spatial light modulators; (110.0110) Imaging systems; (060.5060) Phase modulation.

References and links

1. G. Popescu, *Quantitative Phase Imaging of Cells and Tissues*, Biophotonics (Mcgraw-Hill, 2011).
2. A. Atalar, C. F. Quate, and H. K. Wickramasinghe, "Phase imaging in reflection with the acoustic microscope," Appl. Phys. Lett. **31**(12), 791–793 (1977).
3. C. J. Sheppard and T. Wilson, "Fourier imaging of phase information in scanning and conventional optical microscopes," Philos. Trans. R. Soc. London, Ser. A **295**, 513–536 (1980).
4. T. E. Gureyev and K. A. Nugent, "Rapid quantitative phase imaging using the transport of intensity equation," Opt. Commun. **133**(1-6), 339–346 (1997).
5. T. Ikeda, G. Popescu, R. R. Dasari, and M. S. Feld, "Hilbert phase microscopy for investigating fast dynamics in transparent systems," Opt. Lett. **30**(10), 1165–1167 (2005).
6. G. Popescu, L. P. Deflores, J. C. Vaughan, K. Badizadegan, H. Iwai, R. R. Dasari, and M. S. Feld, "Fourier phase microscopy for investigation of biological structures and dynamics," Opt. Lett. **29**(21), 2503–2505 (2004).
7. E. Cuche, F. Bevilacqua, and C. Depeursinge, "Digital holography for quantitative phase-contrast imaging," Opt. Lett. **24**(5), 291–293 (1999).
8. C. Joo, T. Akkin, B. Cense, B. H. Park, and J. F. de Boer, "Spectral-domain optical coherence phase microscopy for quantitative phase-contrast imaging," Opt. Lett. **30**(16), 2131–2133 (2005).
9. K. Creath and G. Goldstein, "Dynamic quantitative phase imaging for biological objects using a pixelated phase mask," Biomed. Opt. Express **3**(11), 2866–2880 (2012).
10. P. Bon, G. Maucort, B. Wattellier, and S. Monneret, "Quadriwave lateral shearing interferometry for quantitative phase microscopy of living cells," Opt. Express **17**(15), 13080–13094 (2009).
11. C. Mann, L. Yu, C.-M. Lo, and M. Kim, "High-resolution quantitative phase-contrast microscopy by digital holography," Opt. Express **13**(22), 8693–8698 (2005).
12. E. Wolf, *Progress in Optics* (Elsevier Science, 2012), Vol. 57.
13. Z. Wang, L. Millet, V. Chan, H. F. Ding, M. U. Gillette, R. Bashir, and G. Popescu, "Label-free intracellular transport measured by spatial light interference microscopy," J. Biomed. Opt. **16**(2), 026019 (2011).
14. R. Wang, Z. Wang, J. Leigh, N. Sobh, L. Millet, M. U. Gillette, A. J. Levine, and G. Popescu, "One-dimensional deterministic transport in neurons measured by dispersion-relation phase spectroscopy," J. Phys. Condens. Matter **23**(37), 374107 (2011).
15. G. Popescu, Y. Park, N. Lue, C. Best-Popescu, L. Deflores, and R. R. Dasari, "Optical imaging of cell mass and growth dynamics," Am J. Physiol. **295**, 538–544 (2008).
16. M. Mir, Z. Wang, Z. Shen, M. Bednarz, R. Bashir, I. Golding, S. G. Prasanth, and G. Popescu, "Optical measurement of cycle-dependent cell growth," Proc. Natl. Acad. Sci. U.S.A. **108**(32), 13124–13129 (2011).
17. Y. Park, C. A. Best, K. Badizadegan, R. R. Dasari, M. S. Feld, T. Kuriabova, M. L. Henle, A. J. Levine, and G. Popescu, "Measurement of red blood cell mechanics during morphological changes," Proc. Natl. Acad. Sci. U.S.A. **107**(15), 6731–6736 (2010).

#192439 - $15.00 USD Received 17 Jun 2013; revised 25 Jul 2013; accepted 30 Jul 2013; published 8 Aug 2013

18. Z. Wang, D. L. Marks, P. S. Carney, L. J. Millet, M. U. Gillette, A. Mihi, P. V. Braun, Z. Shen, S. G. Prasanth, and G. Popescu, "Spatial light interference tomography (SLIT)," Opt. Express **19**(21), 19907–19918 (2011).
19. W. Choi, C. Fang-Yen, K. Badizadegan, S. Oh, N. Lue, R. R. Dasari, and M. S. Feld, "Tomographic phase microscopy," Nat. Methods **4**(9), 717–719 (2007).
20. Z. Wang, I. S. Chun, X. Li, Z.-Y. Ong, E. Pop, L. Millet, M. Gillette, and G. Popescu, "Topography and refractometry of nanostructures using spatial light interference microscopy," Opt. Lett. **35**(2), 208–210 (2010).
21. Z. Wang, K. Tangella, A. Balla, and G. Popescu, "Tissue refractive index as marker of disease," J. Biomed. Opt. **16**(11), 116017 (2011).
22. B. Bhaduri, H. Pham, M. Mir, and G. Popescu, "Diffraction phase microscopy with white light," Opt. Lett. **37**(6), 1094–1096 (2012).
23. G. Popescu, T. Ikeda, R. R. Dasari, and M. S. Feld, "Diffraction phase microscopy for quantifying cell structure and dynamics," Opt. Lett. **31**(6), 775–777 (2006).
24. Z. Wang, L. J. Millet, M. Mir, H. Ding, S. Unarunotai, J. A. Rogers, M. U. Gillette, and G. Popescu, "Spatial light interference microscopy (SLIM)," Opt. Express **19,** 1016–1026 (2011).
25. D. Zicha and G. A. Dunn, "An Image-Processing System For Cell Behavior Studies In Subconfluent Cultures," J. Microsc. **179**(1), 11–21 (1995).
26. W. C. Warger 2nd and C. A. DiMarzio, "Computational signal-to-noise ratio analysis for optical quadrature microscopy," Opt. Express **17**(4), 2400–2422 (2009).
27. M. Young, B. Faulkner, and J. Cole, "Resolution in optical systems using coherent illumination," J. Opt. Soc. Am. **60**(1), 137–139 (1970).
28. J. W. Goodman, *Speckle phenomena in optics: theory and applications* (Roberts & Co, 2007).
29. D. Paganin and K. A. Nugent, "Noninterferometric phase imaging with partially coherent light," Phys. Rev. Lett. **80**(12), 2586–2589 (1998).
30. A. Yariv and P. Yeh, *Optical waves in crystals* (Wiley New York, 1984), Vol. 5.
31. K. Lu and B. E. A. Saleh, "Theory and design of the liquid crystal TV as an optical spatial phase modulator," Opt. Eng. **29**, 240–244 (1989).
32. J. L. Pezzaniti and R. A. Chipman, "Phase-only modulation of a twisted nematic liquid-crystal TV by use of the eigenpolarization states," Opt. Lett. **18**(18), 1567–1569 (1993).
33. T. H. Barnes, T. Eiju, K. Matusda, and N. Ooyama, "Phase-only modulation using a twisted nematic liquid crystal television," Appl. Opt. **28**(22), 4845–4852 (1989).
34. N. Konforti, E. Marom, and S.-T. Wu, "Phase-only modulation with twisted nematic liquid-crystal spatial light modulators," Opt. Lett. **13**(3), 251–253 (1988).
35. Z. Yin, K. Li, T. Kanade, and M. Chen, "Understanding the optics to aid microscopy image segmentation," in *Medical Image Computing and Computer-Assisted Intervention–MICCAI 2010* (Springer, 2010), pp. 209–217.

1. Introduction

Quantitative Phase Imaging (QPI) [1] has been the subject of intense studies over the past decades [2–11] thanks to its ability to offer intrinsic quantitative information on the optical path length across the imaging sample (see [12], Ch. 3, for a short review). This quantity is proportional to the refractive index difference times the thickness of the sample. Such information has found useful applications in biology (studying mass transport [13, 14], cell growth [15, 16], cell structures and dynamics [6, 17]), tomography [18, 19], topography and refractometry [20], or pathology ([21]). Performance of a QPI system is characterized by four different factors: (a) acquisition rate, (b) transverse resolution (c) spatial phase sensitivity and (d) temporal phase sensitivity [see Chap. 2 in Ref. 1]. The fastest acquisition rate is given by single-shot methods [22, 23] with possible transverse resolution loss (from the theoretical limit). Phase-shifting methods [24–26], on the contrary, retain this limit at the cost of lower frame rate. However, even with phase-shifting method, the theoretical resolution limit can hardly be achieved in practice due to speckle, as a result of high temporal coherence of laser illumination sources [27, 28]. Despite potentially being useful in some applications, speckle is a detrimental factor to the spatial phase sensitivity. Fortunately, white-light methods [24, 29] can remove these speckles almost completely due to an extremely short coherence length (typically in the order of 1 micron). Hence, spatial phase sensitivity is best with white-light methods. Finally, the temporal phase sensitivity attains it maximum performance with common-path methods [6, 22].

The SLIM method, first introduced in [24], combines key strength of the aforementioned methods by using white-light illumination in a phase-shifting manner with common-path geometry to obtain speckle-free phase information with sub-nanometer noise level. Compare to other methods, such as the single-shot pixelated phase masks methods from the 4D

#192439 - $15.00 USD Received 17 Jun 2013; revised 25 Jul 2013; accepted 30 Jul 2013; published 8 Aug 2013

Technology corporation [9], SLIM offers better depth-sectioning capability up to about 1.2 microns thanks to its extremely short temporal coherence length of white light. It also has very good noise sensitivity due to common-path geometry. Compare to the 4-wave lateral shearing interferometry method by Phasics [10], at the cost of lower frame rate, SLIM can retain the lateral resolution at lower computational cost and is more robust against noise. In contrast with the Intensity Transport Equation (ITE) method by IATIA vision [4], SLIM has no assumption on the imaging field and has better axial sectioning. From application standpoint, many other phase imaging methods require dedicated microscopes for phase imaging while SLIM is implemented as an add-on module to traditional microscopes. This makes SLIM very easy to deploy and the research is easily reproducible. So far, SLIM has operated using a parallel aligned LC SLMs (or PAN-SLMs for short) with very high diffraction efficiency. Furthermore, these SLMs are able to perform phase-only modulation without significant intensity attenuation. However, the high cost of the PAN-SLM may represent an obstacle to popularizing SLIM to biomedical users. In an effort to alleviate this issue, here we propose to use the TNLC-SLM as an alternative. This paper demonstrates a SLIM system using a transmission TNLC-SLM from Holoeye's. We show that by simple post-processing steps, the phase information can be recovered from phase-intensity coupled modulations with competitive sensitivity. Besides, we also briefly discuss our optimization calculation to deal with the low diffraction efficiency and optical fill factor of the TNLC-SLM.

The structure of the paper is as follows. In Section 2, we briefly review the TNLC-SLMs in comparison with PAN-SLMs. Section 3 is reserved for describing the optical setup, operation principles, SLM calibration and implementation issues. Experimental results are shown in Section 4. We conclude the paper with Section 5.

2. Review on characteristics of TNLC-SLMs

Two dimensional SLMs is a general term indicating devices that can modulate phase, amplitude and polarization of an optical field. Many of these SLMs are made of a nematic LC cell sandwiched between two transparent addressable electrode arrays. The cell is made of a thin layer of a nematic LCs situated between two rubbed glass plates. The glass walls are polished in pre-determined directions to align the LC molecules. In TNLC-SLMs, these directions are different (usually orthogonal or at 45° to each other). Therefore, the LCs inside the cell gradually rotate helically around the optical axis so that it can match with the polished direction at both ends (see Fig. 1(a)). Meanwhile, for PAN-SLMs or vertical aligned nematic LC-SLMs (VAN-SLM for short), all molecules are parallel to each other due to a unique polishing direction on both walls.

Due to its twisting property, the TNLC-SLM acts as both a phase retarder and a polarization rotator. Under an applied electric field in the z-direction, the LC tilts toward the electrodes, add more phase modulation but gradually lose its twisting properties (see Fig. 1(b)). Thus, pure-phase modulation without polarization rotation and amplitude modulation is not achievable with the TNLC-SLMs. For a TNLC-SLM with a twisting angle ϕ_d, its behavior can be described by the Jones matrix [30]

$$\mathbf{J} = \exp\left(-i\beta_d\right)\mathbf{R}\left(-\phi_d\right)\mathbf{M}\left(\phi_d, \beta_d\right). \tag{1}$$

Here, β_d is the birefringence of the LC cell, defined as $\beta_d = \left(\pi d/\lambda\right)\left[n_e\left(V\right) - n_{o,d}\right]$, where d is the cell thickness, λ is the wavelength of the illumination, $n_e\left(V\right), n_{o,d}$ are the refractive indices of the LC molecules along the extraordinary and ordinary axes when a voltage V is applied. As a side note, here, we use the little subscript "d" to indicate the physical parameters of the TNLC-SLM since notations without "d" will be used to indicate other parameters of

#192439 - $15.00 USD Received 17 Jun 2013; revised 25 Jul 2013; accepted 30 Jul 2013; published 8 Aug 2013
(C) 2013 OSA

more interest in subsequent sections. The second term, $\mathbf{R}(-\phi_d)$, characterizes the twisting effect of the SLM by rotating the polarization around the z-axis by an amount of ϕ_d. The last component, $M(\phi_d, \beta_d)$ introduces an amplitude attenuation and possible extra phase modulation. This component is given as

$$M(\phi_d, \beta_d) = \begin{bmatrix} \cos(\gamma) - i\dfrac{\beta_d}{\gamma}\sin(\gamma) & \left(\dfrac{\phi_d}{\gamma}\right)\sin(\gamma) \\ -\left(\dfrac{\phi_d}{\gamma}\right)\sin(\gamma) & \cos(\gamma) + i\dfrac{\beta_d}{\gamma}\sin(\gamma) \end{bmatrix}, \tag{2}$$

with $\gamma = \sqrt{\phi_d^2 + \beta_d^2}$. In order to modulate incoming light (in the z-direction), the TNLC-SLM is typically coupled with another two polarizers (called polarizer and analyzer) as shown in Fig. 2. Here, main axes of these two polarizers form with the x-axis angles of ψ_{in} and ψ_{out} respectively. As a side note, here all the angles are directional angles, which means they are angles from the x-axis to the axis of interest. The positive direction is counter clockwise (CCW). By Jones calculus, the intensity transmittance (T) and the phase shift (δ) is obtained as [31]

$$T = \cos^2(\psi_{in})\left\{\left[-\frac{\phi_d}{\gamma}\sin(\gamma)\cos(\psi_{in} - \psi_{out}) + \cos(\gamma)\sin(\psi_{in} - \psi_{out})\right]^2 + \left[\frac{\beta_d}{\gamma}\sin(\gamma)\sin(\psi_{in} + \psi_{out})\right]^2\right\}, \tag{3}$$

$$\delta = \beta_d - \tan^{-1}\left[\frac{(\beta_d/\gamma)\sin(\gamma)\sin(\psi_{in} + \psi_{out})}{(-\phi_d/\gamma)\sin(\gamma)\cos(\psi_{in} - \psi_{out}) + \cos(\gamma)\sin(\psi_{in} - \psi_{out})}\right]. \tag{4}$$

For illustration, we show simulated characteristics of a TNLC-SLM (with twisted angle $\phi_d = -90^o$) in two different modes: $\psi_{in} = 45^o, \psi_{out} = -45^o$ (mode 1) and $\psi_{in} = 0^o$, $\psi_{out} = -45^o$ (mode 2) in Fig. 3 and Fig. 4. These characteristics are shown as functions of β_d (from 0 to 2π). Mode 1 is further utilized and discussed in subsequent sections.

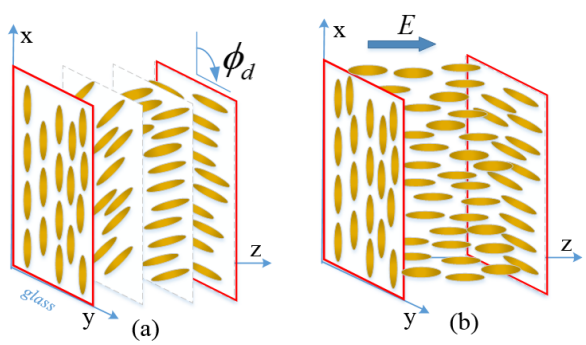

Fig. 1. Twisted nematic LCs in 2 cases. (a) Without applied electric field. (b) Under applied electric field. The molecules tilt towards the electrodes and lose their rotating power.

#192439 - $15.00 USD Received 17 Jun 2013; revised 25 Jul 2013; accepted 30 Jul 2013; published 8 Aug 2013

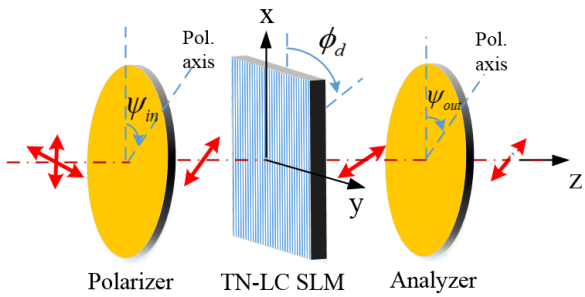

Fig. 2. An example setup for light modulation with TNLC- SLM. A TNLC-SLM is placed between two polarizers (called the polarizer and the analyzer).

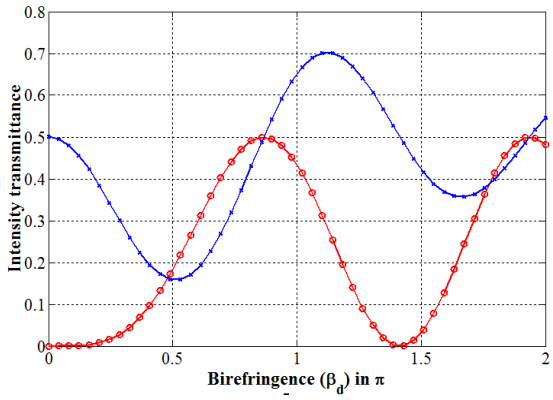

Fig. 3. Intensity transmittance

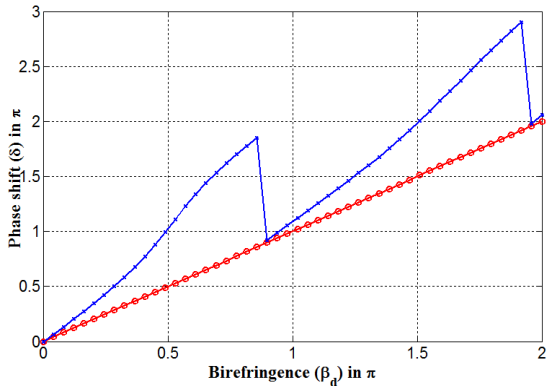

Fig. 4. Phase shifting

#192439 - $15.00 USD Received 17 Jun 2013; revised 25 Jul 2013; accepted 30 Jul 2013; published 8 Aug 2013

3. Optical setup and calibration

3.1 Optical setup & principle of operation

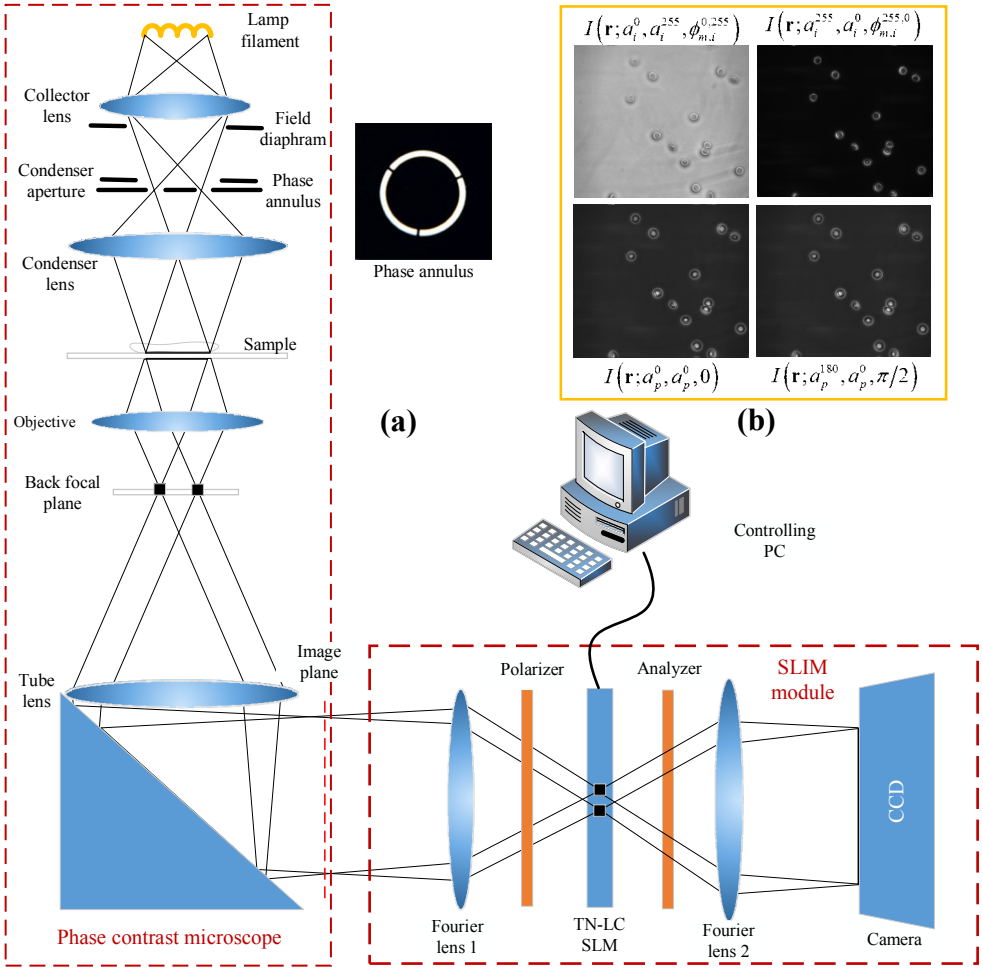

Fig. 5. (a) Optical setup of the SLIM system using TNLC-SLM. The output image from an inverted phase contrast microscope (Nikon Ti-E in our case) is spatially Fourier transformed by Fourier lens 1 onto the surface of a transmission TNLC-SLM (LC 2002 from Holoeye). The SLM introduces different phase and intensity modulations to the Fourier transform of the scattered and non-scattered components. Then, Fourier lens 2 performs a secondary Fourier transform, which reconstructs the image on the LCD. This image plane is conjugated with the sample plane. Since we are using a $40\times/0.95$ NA Plan Apo phase objective with an extra unity magnification from the SLIM module, we have approximately 4.5 pixels per micron (b) Four recorded frames of a SLIM quantitative phase image. Top row: 2 frames recorded under intensity modulation, bottom row: 2 frames recorded under phase-mostly modulation (details of these modes will be discuss later on). Since a phase objective, instead of a bright field one, is used in our acquisition, $I\left(\mathbf{r};a_p^0,a_p^0,0\right)$ corresponds to the phase contrast image and $I\left(\mathbf{r};a_p^{180},a_p^0,\pi/2\right)$ will be an image when the scattered and non-scatter component are 180° out of phase. The field of view has size of size $200\times200\,\mu\text{m}^2$.

Figure 5 displays our optical setup. The caption contains a brief description of our system. Similar to the original SLIM setup [24], we spatially decompose the complex field at the

#192439 - $15.00 USD Received 17 Jun 2013; revised 25 Jul 2013; accepted 30 Jul 2013; published 8 Aug 2013
(C) 2013 OSA

output port of the microscope to a non-scattered component $U_o(\mathbf{r},t)$ and a scattered one $U_1(\mathbf{r},t)$ using a Fourier transform lens. The complex field can be written as

$$U(\mathbf{r},t) = U_o(\mathbf{r},t) + U_1(\mathbf{r},t), \tag{5}$$

where $\mathbf{r} = (\mathrm{x},\mathrm{y})$. Here, $U(\mathbf{r},\mathrm{t})$ is a random fluctuation in the space-time domain. When the coherence area is larger than the field of view, the spatial varying component of this complex field can be defined over the region of interest for any instance of the time t. In other way, $U(\mathbf{r},\mathrm{t})$ can be factorized as $U(\mathbf{r},\mathrm{t}) = U(\mathbf{r})U(t)$ where $U(t)$ denotes the random time varying part of the field, $U(\mathbf{r})$ is the deterministic counterpart that specifies the deterministic phase of interest. From Eq. (5), we have $U(\mathbf{r}) = U_o(\mathbf{r}) + U_1(\mathbf{r})$. Here, $U(\mathbf{r})$ provides a quantitative image of the optical path length variation as

$$\phi(\mathbf{r}) \triangleq \angle U(\mathbf{r}) = \frac{\langle\omega\rangle}{c}\int_o^{h(\mathbf{r})}\left[n(\mathbf{r},z) - n_o\right]dz. \tag{6}$$

In Eq. (6), $n(\mathbf{r},z) - n_o$ is the refractive index difference between the location $(\mathbf{r},z)$ and the surrounding medium, $\langle\omega\rangle, h(\mathbf{r})$ are mean angular frequency and the sample thickness at the transverse location $\mathbf{r}$. When a relative time-delay τ and amplitude modulation factors a_o, a_1, respectively are introduced to each component U_o, U_1, under stationarity assumption, intensity at the detector is

$$\begin{aligned} I(\mathbf{r};a_o,a_1,\phi_m) &= \left\langle \left|a_o U_o(\mathbf{r},t) + a_1 U_1(\mathbf{r},t+\tau)\right|^2 \right\rangle_t \\ &= a_o^2\left|U_o(\mathbf{r})\right|^2 + a_1^2\left|U_1(\mathbf{r})\right|^2 + 2a_o a_1\left|U_o(\mathbf{r})U_1(\mathbf{r})\right|\cos\left[\Delta\phi(\mathbf{r}) + \phi_m\right], \end{aligned} \tag{7}$$

where $\Delta\phi(\mathbf{r}) \triangleq \angle U_1(\mathbf{r}) - \angle U_0(\mathbf{r})$ is the phase difference between the scattered and unscattered components; $\phi_m \triangleq \langle\omega\rangle\tau_m$ is the delay induced by the SLM. Then, $\phi(\mathbf{r})$ can be calculated from $\beta(\mathbf{r}) \triangleq \left(\left|U_1(\mathbf{r})\right| / \left|U_0(\mathbf{r})\right|\right)$ and $\Delta\phi(\mathbf{r})$ by a simple relation (see [6] for more details)

$$\phi(\mathbf{r}) = \tan^{-1}\left(\frac{\beta(\mathbf{r})\sin\left[\Delta\phi(\mathbf{r})\right]}{1 + \beta(\mathbf{r})\cos\left[\Delta\phi(\mathbf{r})\right]}\right). \tag{8}$$

Since we have 3 unknowns in Eq. (7) with two sign possibilities for $\Delta\phi(\mathbf{r})$, 4 modulations with 4 different sets of (a_o, a_1, ϕ_m) are needed. In the next two subsections, we present a method to obtain $\beta(\mathbf{r}), \Delta\phi(\mathbf{r})$ by alternating between two different modulation modes of the TNLC-SLM (each providing two frames). We further discuss implementation issues of our system.

3.2 Image acquisition procedure

Let us use the name "intensity mode" for Mode 1 in Section 2 since this mode offers a large value for the maximum intensity transmittance. We also use the term "phase mode" to indicate the modulation mode when $\psi_{in} = 330^o, \psi_{out} = 0^o$. In this mode, we obtain a $\pi/2$ modulation of the phase (see Fig. 7). The effect of amplitude attenuation is also considered in

#192439 - $15.00 USD Received 17 Jun 2013; revised 25 Jul 2013; accepted 30 Jul 2013; published 8 Aug 2013
(C) 2013 OSA

the calculation. Our calibrations show that for white light, a maximum contrast ratio of 21.15:1 can be obtained by switching the grayscale values g between 250 and 0 in the intensity mode (mode 1). Although this contrast value is not as large as that for a laser, an interference measurement for $I(\mathbf{r})$ when the a_o^2/a_1^2 equals to this contrast (or its reciprocal) can be considered to have only 1 field component. Next, let us use $a_i^g, \phi_{m,i}^{g_0,g_1}$ to indicate the amplitude attenuation factors when the grayscale, g, is applied and the relative modulated phase when grayscale values g_0, g_1 are applied to each field U_o, U_1 simultaneously. Here, the subscript i indicates the intensity modulation mode, to differentiate with the p subscript for the phase mode. In intensity mode, we have,

$$\left.\begin{aligned} I\left(\mathbf{r};a_i^0,a_i^{255},\phi_{m,i}^{0,255}\right) &\approx \left(a_i^{255}\right)^2\left|U_1(\mathbf{r})\right|^2 \\ I\left(\mathbf{r};a_i^{255},a_i^0,\phi_{m,i}^{255,0}\right) &\approx \left(a_i^{255}\right)^2\left|U_0(\mathbf{r})\right|^2 \end{aligned}\right\} \Rightarrow \beta(\mathbf{r}) \approx \sqrt{\frac{I\left(\mathbf{r};a_i^0,a_i^{255},\phi_{m,i}^{0,255}\right)}{I\left(\mathbf{r};a_i^{255},a_i^0,\phi_{m,i}^{255,0}\right)}}. \tag{9}$$

Given $\beta(\mathbf{r})$ calculated from Eq. (9), the next task is calculating $\Delta\phi(\mathbf{r})$. To do this, we switch to the phase modulation mode, where a phase shift of $\phi_m = \pi/2$ can be easily introduced by setting $g_0 = 180,\ g_1 = 0$. Setting $g_1 = g_2 = 0$ and $g_0 = 180, g_1 = 0$ gives

$$\begin{aligned} I\left(\mathbf{r};a_p^0,a_p^0,0\right) &\approx \left(a_p^0\right)^2\left|U_0(\mathbf{r})\right|^2 + \left(a_p^0\right)^2\left|U_1(\mathbf{r})\right|^2 + 2\left(a_p^0 a_p^0\right)\left|U_0(\mathbf{r})U_1(\mathbf{r})\right|\cos\left(\Delta\phi(\mathbf{r})\right), \\ I\left(\mathbf{r};a_p^{180},a_p^0,\frac{\pi}{2}\right) &\approx \left(a_p^{180}\right)^2\left|U_0(\mathbf{r})\right|^2 + \left(a_p^0\right)^2\left|U_1(\mathbf{r})\right|^2 - 2\left(a_p^{180} a_p^0\right)\left|U_0(\mathbf{r})U_1(\mathbf{r})\right|\sin\left(\Delta\phi(\mathbf{r})\right). \end{aligned} \tag{10}$$

Equation (10) results in

$$\frac{I\left(\mathbf{r};a_p^0,a_p^0,0\right)}{I\left(\mathbf{r};a_p^{180},a_p^0,\pi/2\right)} = \frac{\left(a_p^0\right)^2 + \left(a_p^0\right)^2\beta(\mathbf{r})^2 + 2\left(a_p^0 a_p^0\right)\beta(\mathbf{r})\cos\left(\Delta\phi(\mathbf{r})\right)}{\left(a_p^{180}\right)^2 + \left(a_p^0\right)^2\beta(\mathbf{r})^2 - 2\left(a_p^{180} a_p^0\right)\beta(\mathbf{r})\sin\left(\Delta\phi(\mathbf{r})\right)}, \tag{11}$$

where $\Delta\phi(\mathbf{r})$ can be solved clearly by substituting Eq. (9) into Eq. (11). As a side note, we measured the modulation coefficients in advanced and stored in the memory for efficient computing. We summary our modulation procedures for a single phase acquisition are summarized in Table 1.

Table 1. Modulation procedure for SLIM with TNLC-SLM for a single phase acquisition

• Set the polarizers into the intensity modulation mode $\psi_{in} = 45^o, \psi_{out} = -45^o$.
• Acquire $I\left(\mathbf{r};a_i^0,a_i^{255},\phi_{m,i}^{0,255}\right)$, $I\left(\mathbf{r};a_i^{255},a_i^0,\phi_{m,i}^{255,0}\right)$ and calculate $\beta(\mathbf{r})$ using Eq. (9).
• Switch the polarizers into the phase modulation mode $\psi_{in} = 330^o, \psi_{out} = 0^o$.
• Obtain $I\left(\mathbf{r};a_p^0,a_p^0,0\right)$, $I\left(\mathbf{r};a_p^{180},a_p^0,\pi/2\right)$, combine with $\beta(\mathbf{r})$ to compute $\Delta\phi(\mathbf{r})$ as given in Eq. (11).
• Use $\beta(\mathbf{r})$ and $\Delta\phi(\mathbf{r})$ to compute $\phi(\mathbf{r})$ in Eq. (8).

#192439 - $15.00 USD Received 17 Jun 2013; revised 25 Jul 2013; accepted 30 Jul 2013; published 8 Aug 2013

3.3 TNLC-SLM calibration procedures

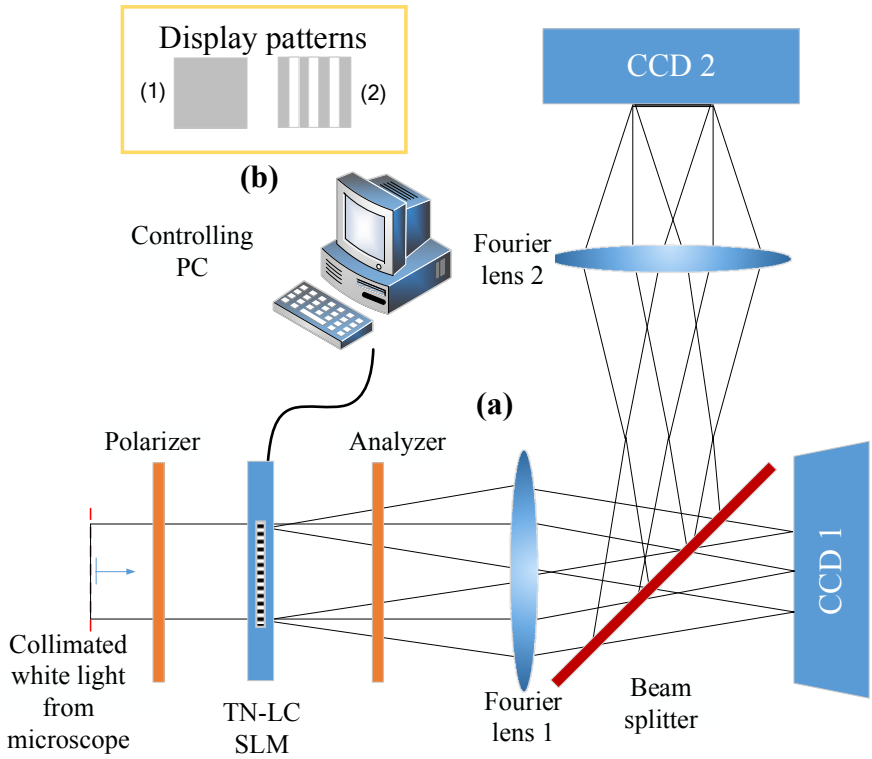

Fig. 6. (a) Optical setup for TN-LC SLM calibration. (b) Two SLM patterns used in the calibration.

Since the TNLC-SLM is designed to work with the laser, not for white light, extra calibration steps are needed to ensure proper operations. Figure 6(a) shows our optical setup for TNLC-SLM calibration. Here, we use the CCD camera 1 to image the diffraction pattern and CCD camera 2 to image the SLM plane. In order to calculate intensity transmittance, we project different homogeneous patterns with different grayscales values g (pattern (1) in Fig. 6(b)). The relative amplitude attenuation factors are given by $r^{g,0} = \left(a^g / a^o\right) = \sqrt{\left\langle I_2^{g,(1)}(\mathbf{r})\right\rangle_{\mathbf{r}} / \left\langle I_2^{0,(1)}(\mathbf{r})\right\rangle_{\mathbf{r}}}$, where $I_2^{g,(1)}(\mathbf{r})$ is the intensity image on camera 2 when pattern (1) with grayscale value g is projected. As a side note, here, the formula applies to all operation modes of the TNLC-SLM. Therefore, it is not necessary to add the indices i or p. To determine the relative modulated phase shift $\phi_m^{g,0}$, we project the 50/50 grating pattern (pattern (2) in Fig. 6(b)) which interlaces between the grayscale value g and 0. By some simple calculations, the intensity value at the zero-diffraction order on CCD1, when pattern (2) is used, is given as $I_1^{g,(2)} = I_1^{0,(2)}\left[1 + \left(r^{g,0}\right)^2 + 2r^{g,0}\cos\left(\phi_m^{g,0}\right)\right]/4$, from which $\phi_m^{g,0}$ can be determined numerically. To further determine whether $\phi_m^{g,0} \in [0,\pi]$ or $[\pi, 2\pi]$, we determine whether the relative modulated phase has crossed π or not. We also fit our measurements with a simulated modulated phase curve for different wavelength (in Section 2) for consistency validation. Here, $I_1^{g,(2)}$ is the intensity image on camera 1 when the pattern (2) is projected with by interlacing stripes of grayscale values g and 0.

#192439 - $15.00 USD Received 17 Jun 2013; revised 25 Jul 2013; accepted 30 Jul 2013; published 8 Aug 2013
(C) 2013 OSA

3.4 Design consideration

Several attempts have been spent on finding phase-only modulation configurations for the TNLC-SLMs (see [32–34] and other references therein). Unfortunately, these systems are designed for (quasi-) monochromatic sources and there is no performance guarantee for broad band illumination (e.g. white light). Therefore, a simple setup where all the effects of phase-intensity coupling is accounted and compensated is strongly preferred. Thus, we simplified our system as much as possible and corrected for the amplitude attenuation effect inherent to TNLC.

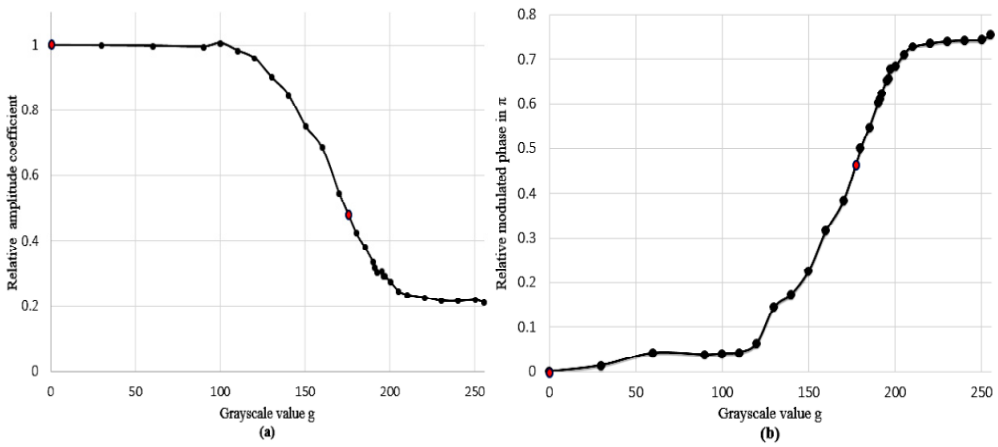

Fig. 7. Measured modulation characteristics for the phase-mostly modulation mode $\psi_{in} = 330^{\circ}, \psi_{out} = 0^{\circ}$. Red dots indicate operating points that are used in the SLIM measurements (see Table 1). (a) Relative amplitude modulation factor $r^{g,0}$ vs. grayscale value g. (b) Relative modulated phase shift $\phi_m^{g,0}$ vs. grayscale values g.

We alternate between two modulation modes within a single acquisition. As a result, we utilize the fact that the amplitude of each field can be obtained directly from a single measurement in the intensity mode thanks to its high contrast ratio. Next, due to the lack of a dielectric mirror layer, which is typically available in reflection PAN-SLM, and a much smaller aperture ratio (55% in our LC2002 SLM), the TNLC-SLM have a significantly smaller diffraction efficiency than that of the PAN-SLM. In other way, the first-order diffraction has a non-negligible effect on the intensity image at the camera plane of the CCD in our SLIM setup. We minimize this effect by imaging a portion of the full field of view so that there is no overlapping of the zero and the first diffraction order at the CCD plane. For our system, this area has size of $200 \times 200\,\mu m^2$.

4. Results

In order to verify the accuracy of our method, we image polystyrene micro-beads of mean diameter $2\,\mu$m $\pm 5\%$ (CAT #19814, Polysciences Inc.) with a refractive index of $n = 1.5962$ at 550 nm in immersion oil $n = 1.518$ from Zeiss. Figure 8(a) shows an image of two micro-beads with a corresponding cross-section along the line profile in Fig. 8(b). It can be seen that the thickness of the beads correlates very well with our prior knowledge of its diameters.

Next, in order to quantify the spatial phase sensitivity of our system, we record an image of the spatial path length in a background area (with no-sample contribution, just the medium). Figure 8(c) shows an optical path length (OPL) map of this area. Figure 8(d) (red) shows a histogram of corresponding OPL variation. Using the formula

#192439 - $15.00 USD Received 17 Jun 2013; revised 25 Jul 2013; accepted 30 Jul 2013; published 8 Aug 2013
(C) 2013 OSA

$\sigma_s = (c/\langle\omega\rangle)\sqrt{\left\langle\left[\phi(\mathbf{r})-\langle\phi(\mathbf{r})\rangle_{\mathbf{r}}\right]^2\right\rangle_{\mathbf{r}}}$ to calculate the standard deviation of the spatial OPL variation, we get $\sigma_s = 0.99$ nm. Here, $\langle . \rangle_{\mathbf{r}}$ denotes averaging over different pixels in imaging area.

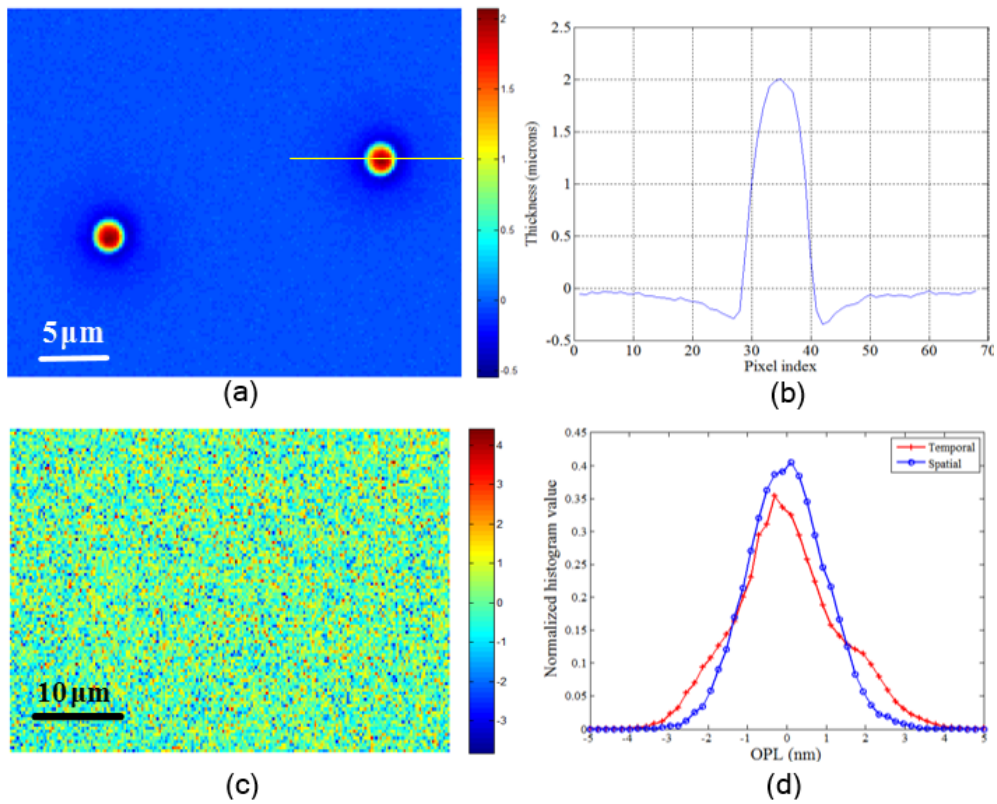

Fig. 8. (a) Thickness map (in microns) of two polystyrene micro-beads of $2\,\mu m$ mean diameter. (b) Cross-section along the line profile in (a). Horizontal axis shows the pixel indices while the vertical axis shows the thickness. (c) Quantitative optical path length (OPL) map of a background region for a single frame. The unit is in nanometers. (d) Blue: Histogram of optical path length noise of across (c) (standard deviation $\sigma_s = 0.99\ nm$). Red: Histogram of optical path length temporal noise across 284 frames (standard deviation $\sigma_t = 1.33\,nm$).

Another important aspect for phase measurement is the temporal noise analysis. In other to characterize this temporal stability, we record a series of 284 frames of the background over 30 seconds. Then, we perform *common mode* noise removal [1] by subtracting each recorded frame to its temporal average. After this step, the "noise phase image" recorded at location $\mathbf{r}$ and time t is given by $\delta\phi(\mathbf{r},t) \triangleq \phi(\mathbf{r},t)-\phi(\mathbf{r}) = \phi(\mathbf{r},t)-\langle\phi(\mathbf{r},t)\rangle_t$. Here, $\langle . \rangle_t$ denotes the temporal average. Then, the standard deviation of the temporal OPL variation is calculated using $\sigma_t = \langle\sigma_t(\mathbf{r})\rangle_{\mathbf{r}} = (c/\langle\omega\rangle)\left\langle\sqrt{\langle\phi(\mathbf{r},t)^2\rangle_t}\right\rangle_{\mathbf{r}}$, which gives us a value of 1.33 nm. We also show a histogram of the temporal OPL variation in Fig. 8(d) (red). It can be seen that our system obtains an equivalent temporal sensitivity with the Diffraction Phase Microscopy (DPM) technique using white light [22] (1.1 nm temporally) but lower than the original SLIM setup with a PAN-SLM [24] (0.28 nm spatially and 0.029 nm temporally). Apart from pristine

#192439 - $15.00 USD Received 17 Jun 2013; revised 25 Jul 2013; accepted 30 Jul 2013; published 8 Aug 2013

optics and alignment quality, lower values of the spatial and temporal noise OPL deviation can be explained by a lower aperture ratio, 55% for TNLC-SLMs vs. 95% for PAN-SLM (e.g. the XY series SLMs from Boulder Nonlinear system).

Next, we imaged normal red blood cells (RBCs) with our system. The cells were diluted prior to imaging. Figure 9 shows a quantitative phase image that reveals normal discocytic shapes of the cell on a uniform background. Here, the phase is displayed in radians.

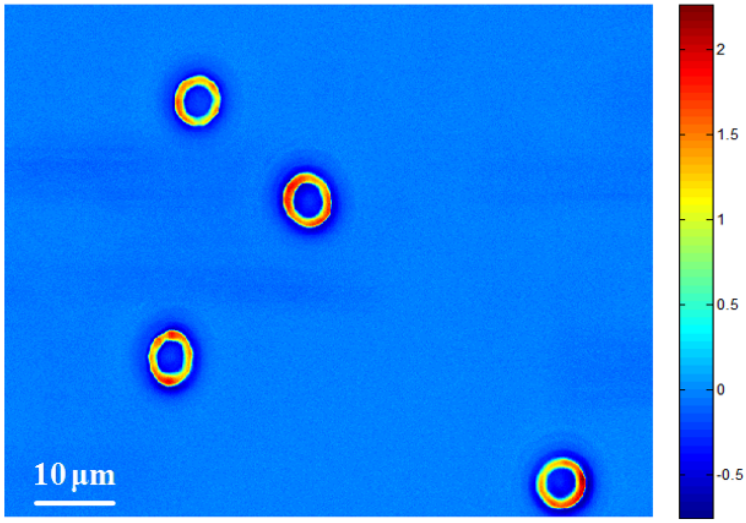

Fig. 9. Quantitative phase image of the red blood cells; colorbar indicates phase in rads.

Finally, we show experimental results with human cancer cervical epithelial (HeLa) cells. The cells were placed on a glass bottom dish and keep in at 37 °C in the incubator for developing to a sufficient confluence. Then, the dish is covered with a cover glass to prevent evaporation before being placed in the microscope stage for imaging. Due to the cells' thickness, different portion of their bodies have different planes of focus. Therefore, it is needed to image across the cells' volume at different z-stacks. Here, we image at z-increment of 0.3 microns, which corresponds to about 3 samples per coherence length. Figure 10 shows our phase contrast images, which are extract frames from a movie (Media 1), side by side with SLIM images at two different z-values $z = 0\mu m$ and $z = 1.8\mu m$. These values are intentionally chosen so that different parts of the cell bodies are visible. Note that our SLIM images also suffer from the halo effects, which is a well-known phenomenon due to the penetration of the scattering light into the modulation phase ring. However, the effect is partially attenuated in our reconstructions due to the combination of 4 frames, which subtract some of the halo effect. This attenuation also reveals finer details (e.g. shaper edge pointed by the red arrows) in our images. We believe that this phenomenon can be fixed by additional numerical post processing steps for each acquired frames [35], or doing optically with possible extra modulations. A movie recording (Media 1) showing acquisition results at different z-stacks is also attached to this paper.

#192439 - $15.00 USD Received 17 Jun 2013; revised 25 Jul 2013; accepted 30 Jul 2013; published 8 Aug 2013

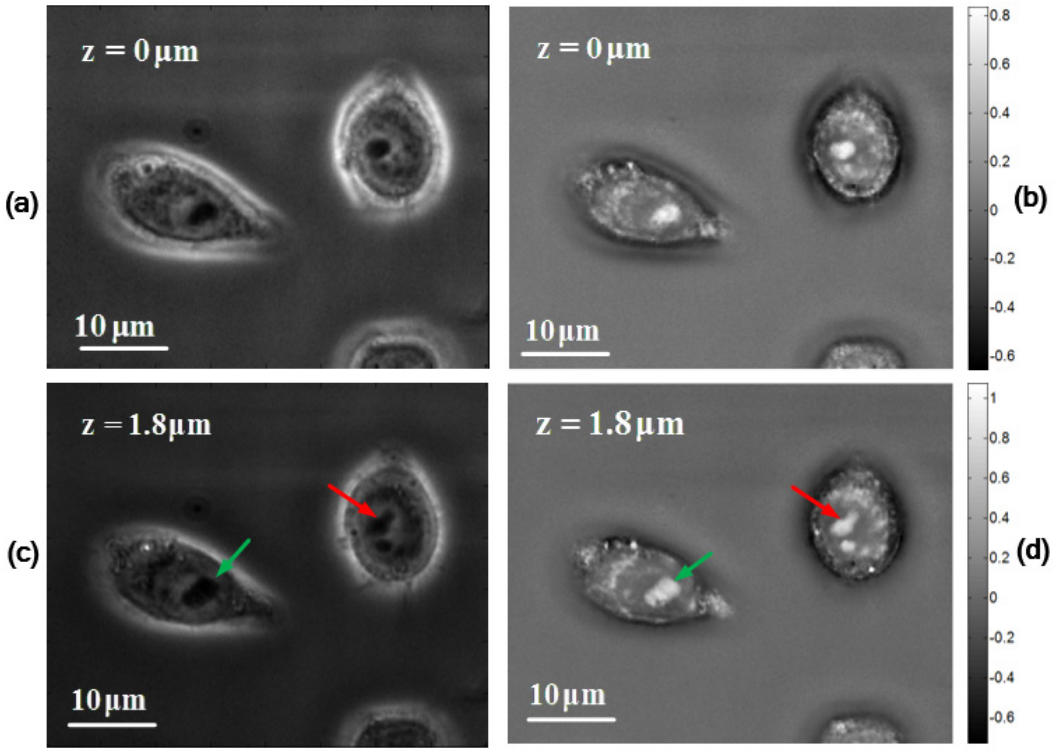

Fig. 10. (a), (b) Phase Contrast and SLIM images of two HeLa cells at one z-stack (chosen as $z = 0\mu m$), (c), (d) Another pair of Phase Contrast and SLIM images of the HeLa cells at $z = 1.8\mu m$. These images are frames extracted from Media 1. The green arrows point to the location of nucleoli. Thanks to combination of 4 frames, the halo effect is SLIM is less than Phase Contrast. This fact subsequently renders higher contrast ratio in SLIM images (e.g. the red arrows points to the location when a shaper edge of the nucleoli is observed) compared to the Phase Contrast images. Color bar indicates phase in radians.

5. Conclusion

In this paper, we demonstrated, for the first time to our knowledge, a quantitative phase imaging system based on SLIM using a TNLC-SLM. The system is able to retain the optical transverse resolution with a spatial and temporal phase sensitivity competitive to DPM. We overcome two obstacles of the TNLC-SLM, which are low diffraction efficiency and strong dispersion, by optimizing the field of view and switching between two modulation modes: intensity and phase-mostly. This switching can be done very fast in practice using a suitable polarization rotator. Thus, acquisition speed is not hindered by the switching. The accuracy of our method is demonstrated by experimental results on micro-beads and biological samples.

Acknowledgment

The authors would like to thanks Taewoo Kim and Shamira Sridharan for maintaining the HeLa cell culture, Hoa Pham for helping with the blood sample preparation and Trang Vu for reviewing the paper. This research was supported by the National Science Foundation (grants CBET 08-46660 CAREER, CBET-1040462 MRI) and Agilent Labs. For more information, visit http://light.ece.uiuc.edu/.